Journal of Materials Chemistry A

Scalable Nanoarchitectonics with Microporous Polymer Composite for Methanol-Tolerant ORR Electrocatalysts†

Journal:	*Journal of Materials Chemistry A*
Manuscript ID	TA-COM-07-2024-004577.R1
Article Type:	Communication
Date Submitted by the Author:	02-Aug-2024
Complete List of Authors:	Sebastian, Abin; National Institute for Materials Science, Research Center for Materials Nanoarchitectonics Panda, Atanu; National Institute for Materials Science, Research Center for Materials Nanoarchitectonics Nandan, Ravi; National Institute for Materials Science, Research Centerfor Materials Nanoarchitectonics Henzie, Joel; National Institute for Materials Science, Research Center for Materials Nanoarchitectonics Cretu, Ovidiu; National Institute for Materials Science, Center for Basic Research on Materials Xu, Jian; National Institute for Materials Science, International Center for Young Scientists Velychkivska, Nadiia; National Institute for Materials Science, Research Center for Materials Nanoarchitectonics Ma, Renzhi; National Institute for Materials Science, Research Center for Materials Nanoarchitectonics Gakhad, Pooja; Indian Institute of Science, Materials Research Centre Singh, Abhishek; Indian Institute of Science, Materials Research Centre Richards, Gary; Shibaura Institute of Technology - Omiya Campus, Chemistry Kimoto, Koji; National Institute for Materials Science Shrestha, Lok Kumar; National Institute for Materials Science, Research Center for Materials Nanoarchitectonics; University of Tsukuba, Department of Materials Science, Institute of Pure and Applied Sciences Ariga, Katsuhiko; National Institute for Materials Science, Research Center for Materials Nanoarchitectonics; The University of Tokyo, Department of Advanced Materials Science, Graduate School of Frontier Sciences Yamauchi, Yusuke; Nagoya University, Department of Materials Process Engineering; Yonsei University, Department of Chemical and Biomolecular Engineering; The University of Queensland Hill, Jonathan; National Institute for Materials Science, Research Center for Materials Nanoarchitectonics

COMMUNICATION

Scalable Nanoarchitectonics with Microporous Polymer Composite for Methanol-Tolerant ORR Electrocatalysts†

Received 00th January 20xx,
Accepted 00th January 20xx

DOI: 10.1039/x0xx00000x

Abin Sebastian[a], Atanu Panda[a], Ravi Nandan[a], Joel Henzie[a], Ovidiu Cretu[b], Jian Xu[c], Nadiia Velychkivska[a], Renzhi Ma[a], Pooja Gakhad[d], Abhishek Kumar Singh[d], Gary J. Richards[e], Koji Kimoto[b], Lok Kumar Shrestha[a,f], Katsuhiko Ariga[a,g], Yusuke Yamauchi[h,i,j], and Jonathan P. Hill*[,a]

Abstract. We report an efficient ORR electrocatalyst containing cobalt single atom and cobalt nanoparticle active sites embedded in a porous nitrogen-doped graphitic carbon network. The robust electrocatalyst exhibits superior electrochemical ORR activity with onset and half-wave potentials of 0.96 V and 0.87 V (*vs*. reversible hydrogen electrode), respectively, and has excellent durability and methanol tolerance further enhancing the potential of this system for practical applications.

The increasing global demand for energy resources, coupled with escalating environmental challenges, has stimulated an intensive research effort in the development of renewable energy conversion and storage technologies, including fuel cells and metal-air batteries, where the cathodic oxygen reduction reaction (ORR) plays a pivotal role.[1,2] However, the poor kinetic characteristics of the available ORR materials have impeded any practical realization of the related applications on an industrial scale. Platinum group metal (PGM) catalysts have been used to address the difficulties associated with ORR operation, but the poor availability and high cost of PGMs make their widespread usage impractical.[3] Based on their low cost, high activities, and excellent stabilities, nitrogen-doped porous carbons incorporating transition metals (Fe, Cu, Co, and Ni) in different states are promising replacement materials for Pt-based ORR systems.[4–10] In these materials, the introduction of different metal-nitrogen (M-Nx) coordination sites is a critical factor in determining their overall efficiency, and also helps establish structure-activity relationships.[11–14] M-Nx coordination sites can be conveniently introduced to the relevant materials by using appropriate coordination complexes such as porphyrins or phthalocyanines, which provide four nitrogen atoms in an M-N_x coordination structure with a suitable geometry not only to bind transition metal cations but also to maintain a state of coordination unsaturation.[15,16] While M-Nx porphyrins and phthalocyanines have been incorporated into different materials for the construction of various composite electrocatalysts,[17–22] there remain several disadvantages associated with this approach including their low affinity for the conductive scaffolds and their strong tendency to aggregate, both of which lead to poor charge and mass transfer rates, low mass efficiency, and low stability of the resulting materials. M-Nx-type molecules can also be incorporated as linkers or monomers in the construction of metal-organic frameworks (MOF),[23,24] covalent organic polymers (COP)[25–29] or covalent organic frameworks (COF).[30,31] Porous porphyrin polymers have also been studied for the construction of M-Nx systems[32–35] with the resulting nitrogen-doped carbon materials being porous and conductive promoting their usefulness in ORR applications. In addition, the use of N-doped graphene supports containing pyridinic N or graphitic N states can enhance the ORR performance of the relevant materials,[36,37] and the use of highly porous conducting carbon supports having numerous exposed active sites facilitates electrocatalytic reactions.

[a.] *Research Center for Materials Nanoarchitectonics (MANA), National Institute for Materials Science (NIMS), Tsukuba 305-0044, Ibaraki, Japan.* E_mail: jonathan.hill@nims.go.jp
[b.] *Center for Basic Research on Materials (CFRM), National Institute for Materials Science (NIMS), Tsukuba 305-0044, Ibaraki, Japan.*
[c.] *International Center for Young Scientists (ICYS), National Institute for Materials Science (NIMS), Tsukuba 305-0044, Ibaraki, Japan.*
[d.] *Materials Research Centre, Indian Institute of Science, Mathikere, Bengaluru, Karnataka 560012, India.*
[e.] *Department of Applied Chemistry, Graduate School of Engineering and Science, Shibaura Institute of Technology, Fukasaku 307, Minuma-ku, Saitama-shi, Saitama 337-8570, Japan.*
[f.] *Department of Materials Science, Institute of Pure and Applied Sciences, University of Tsukuba 1-1-1, Tennodai, Tsukuba 305-8573, Ibaraki, Japan.*
[g.] *Department of Advanced Materials Science, Graduate School of Frontier Sciences, The University of Tokyo, 5-1-5 Kashiwanoha, Kashiwa, Chiba 277-8561, Japan.*
[h.] *Department of Materials Process Engineering, Graduate School of Engineering, Nagoya University, Nagoya 464–8603, Japan.*
[i.] *Department of Chemical and Biomolecular Engineering, Yonsei University, 50 Yonsei-ro, Seodaemun-gu, Seoul 03722, South Korea.*
[j.] *Australian Institute for Bioengineering and Nanotechnology (AIBN) and School of Chemical Engineering, The University of Queensland, Brisbane, Queensland 4072, Australia*
† Electronic Supplementary Information available: See DOI: 10.1039/x0xx00000x

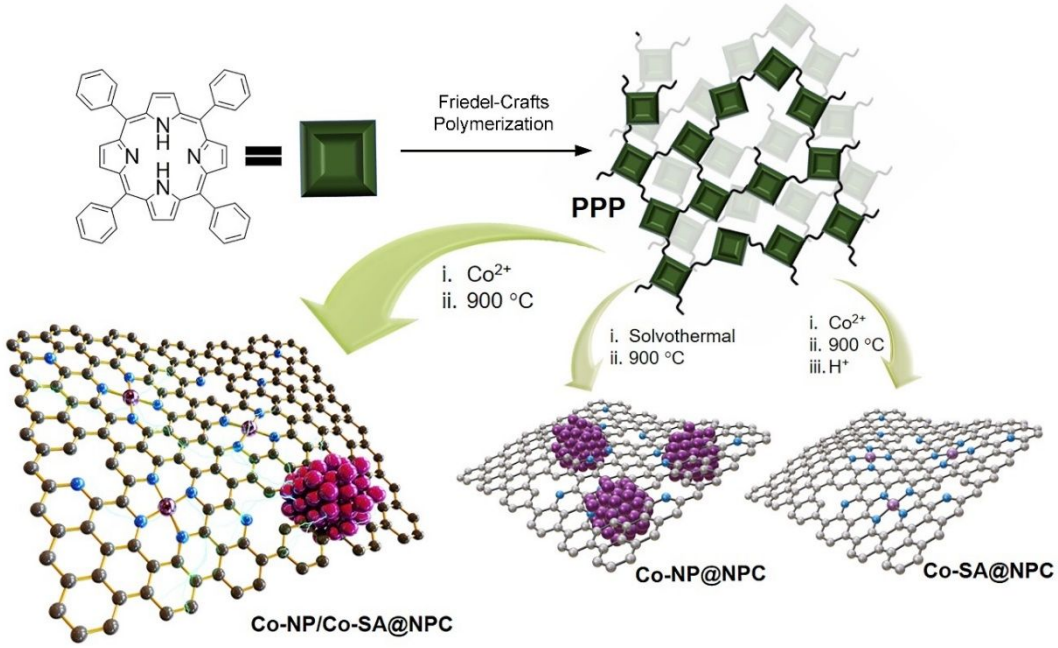

Figure 1. Preparation of cobalt nanoparticle/cobalt single atom catalyst incorporated in nitrogen-doped multilayered graphitic carbon. Tetraphenylporphyrin is polymerized yielding high surface area microporous polmers, which is subsequently processed to the electrocatalyst **Co-NP/Co-SA@NPC** and control materials **Co-NP@NPC** and **Co-SA@NPC**.

Of transition metal-containing materials, cobalt-based electrocatalysts have emerged as leading candidates due primarily to their partially filled d-orbital ($3d^7$) and the possibility of multiple oxidation states (Co^{2+} and Co^{3+}). These features facilitate tuning of electrochemical activity through the preparation of innovative architectures,[38–40] the introduction of heteroatoms (including boron,[41] nitrogen,[42,43] sulfur,[39,44–46] and/or oxygen[47]) or by the preparation of multimetallic systems.[45,48–51] A wide range of cobalt-based nanostructures has been explored to maximize catalytic surface area, increase the density of active sites, and optimize their accessibility for enhanced catalytic performance. In particular, cobalt-based single-atom catalysts (SACs) and metallic clusters or nanoparticles have been widely studied for ORR.[52,53] The construction of Co-SACs with multiple active sites also offers a promising strategy to improve ORR performance, while the use of multiple metal sites (including clusters or nanoparticles) anchored on N-doped carbon substrates allows optimized adsorption-desorption behavior during ORR due to synergistic effects between the metal sites and locally unsymmetrically distributed electron density.[49,52,53] Consequently, the coexistence in the relevant materials of single metal atoms and nanoparticles holds significant potential for the optimization of ORR catalytic performance. However, an easily implementable approach to synthesize these materials based on combining single atom catalysts and metal nanoparticles on conducting N-doped graphene is lacking.

In this work, we have developed a simple synthesis protocol to prepare cobalt-based electrocatalysts based on an inexpensive porous porphyrin polymer precursor. Porous porphyrin polymer containing multiple transition metal binding sites is prepared in high yield using Friedel-Crafts cross-coupling polymerization of meso-tetraphenylporphyrin (TPP). Subsequently, cobalt cations are introduced by coordination in the porphyrin polymer. Controlled thermolysis of the resulting metallated porphyrin polymer results in materials incorporating face-centered cubic (fcc) metallic cobalt nanoparticles (**Co-NP**) as well as cobalt single-atom catalysts (**Co-SA**) confined in porous N-doped graphitic carbon (**NPC**), which has been confirmed by using transmission electron microscopy (TEM), X-ray photoelectron spectroscopy (XPS), and other X-ray absorption techniques (XANES, EXAFS). Of the materials prepared, the **Co-NP/Co-SA@NPC** electrocatalyst exhibits remarkable oxygen reduction reaction (ORR) performance with an onset potential (E_{onset}) of 0.96 V vs RHE and a half-wave potential ($E_{1/2}$) of 0.865 V vs RHE, surpassing the performances of control samples and the state-of-the-art reference material Pt/C (20 wt%). **Co-NP/Co-SA@NPC** catalyst also exhibits substantial methanol tolerance during operation, emphasizing its superiority over Pt/C, and has high durability, making it an excellent candidate for implementation in the relevant applications.

Results and Discussion

Porous porphyrin polymer (PPP) was prepared using meso-tetraphenylporphyrin (TPP) monomer by aryl-aryl Scholl coupling/solvent knitting Friedel-Crafts polymerization using aluminum chloride as Lewis acid catalyst in dichloromethane (See Figure 1).[54] The reaction gives an insoluble brown powder as the product, whose infrared spectrum (FT-IR; Figure S1) contains broadened absorption bands signifying the polymeric structure of PPP. Cobalt cations were introduced to PPP by its reaction with $CoCl_2.6H_2O$ in refluxing DMF yielding PPP-Co

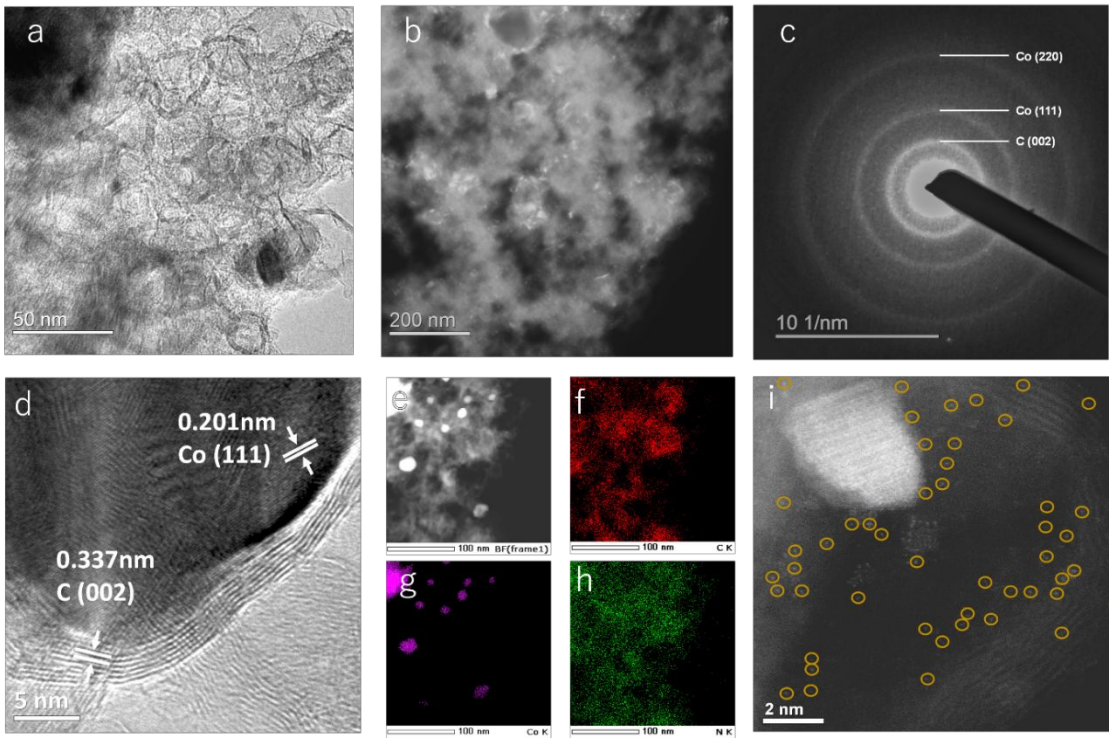

Figure 2. Electron microscopy analyses of **Co-NP/Co-SA@NPC**. (a) Scanning transmission electron microscopy (STEM) image (bright field mode). (b) STEM image (dark field). (c) Selected area electron diffraction (SAED) pattern with indices. (d) High resolution TEM image with important lattice fringes indicated for C and Co. (e) STEM and (f-h) EDX elemental mapping for C (f), Co (g) and N (h) of the area shown in (e). (i) Aberration-corrected high-angle annular dark-field scanning transmission electron microscopy (ac-HAADF-STEM) images of **Co-NP/Co-SA@NPC**. Sites of single Co atoms are marked with yellow circles.

confirmed by the appearance of the characteristic N-Co stretching vibration band at 1004 cm^{-1} in its FTIR spectrum.[55] **PPP-Co** was subjected to thermolysis under constant nitrogen gas flow at different temperatures in the range 500 – 1000 °C. Cobalt nanoparticle (**Co-NP**)/cobalt single atom (**Co-SA**) catalytic sites deposited in nitrogen-doped porous graphitic carbon (**NPC**), **Co-NP/Co-SA@NPC** materials, were obtained upon thermolyzing **PPP-Co** at 1000 °C. Free base porphyrin polymer thermolyzed under the same conditions (**PPP-1000**), cobalt single-atom-only **Co-SA@NPC** and cobalt nanoparticle-only **Co-NP@NPC** (prepared by solvothermal treatment) in nitrogen-doped porous carbon were also prepared as control materials for comparative purposes.

Surface areas and porosities of the materials were measured using nitrogen adsorption/desorption isotherms. (Figure S2a) The relatively large nitrogen adsorption at 77 K at low relative pressure (P/P_0 0.01) for **PPP**, **PPP-Co** indicates that micropores contribute significantly to the total pore volume. Following thermolysis, there is a predictable decline in the surface area due to the partial collapse of the porous structure, although a substantial surface area is retained; **Co-NP/Co-SA@NPC** maintained 478 $m^2\ g^{-1}$ while **PPP-Co** maintained 970 $m^2\ g^{-1}$. Variation in surface area of **Co-NP/Co-SA@NPC** with increasing temperature corresponds approximately to the weight loss according to thermogravimetry (Figure S2b). The excellent acid/base and thermal stability (more than 85% mass remains after pyrolysis) and retention of the porous structure can be attributed to the robust network aromatic polymer structure, which provides an additional advantage over, for instance, materials prepared by direct pyrolysis of the porphyrin monomer.[56] The persistently large surface areas and tailored pore size distributions of the materials (Figure S2c,d) are favorable to promote electrochemical processes, in particular facilitating ion diffusion.

Morphological analyses of the materials are shown in Figure 2 and Figure S3-S5 in the Supporting Information. Scanning electron microscopy (SEM; Figure S3) reveals an irregular aggregated particle structure of the polymers, a morphology that hardly varies during metalation and thermolysis. Transmission electron microscopy (TEM) images (Figure S4) of **PPP-Co** indicate that there are no cobalt nanoparticles present, and selected area electron diffraction (SAED) patterns contain no reflections because the polymers are amorphous with no long-range crystallographic order due to their irregular chemical structure.[26] Energy-dispersive X-ray spectroscopy (EDX; Figure S6) confirms the presence of C, N, and Co distributed uniformly in **PPP-Co**. TEM imaging of **Co-NP/Co-SA@NPC** (Figure 2a) reveals its nanometric porous morphology and the STEM image (Figure 2b) contains bright spots due to the presence of cobalt nanoparticles (**Co-NP**) in the carbon matrix. The selected area electron diffraction (SAED) pattern (Figure 2c) contains (111) and (220) planes assigned to fcc **Co-NP**s. EDX (Figure 2d-g) of **Co-NP/Co-SA@NPC** establishes the presence of Co (apparently in nanoparticulate form) and a uniform distribution of N consistent with the proposed structure: **Co-NP** embedded in N-doped carbon. HR-TEM imaging (Figure 2h) reveals that **Co-NP**s are coated with layers of graphitic carbon and the lattice fringes at 0.34 and 0.20 nm can be assigned to (002) interplane distances of graphitic carbon and the (111) plane of metallic Co, respectively, the latter which supports the formation of **Co-NP**.

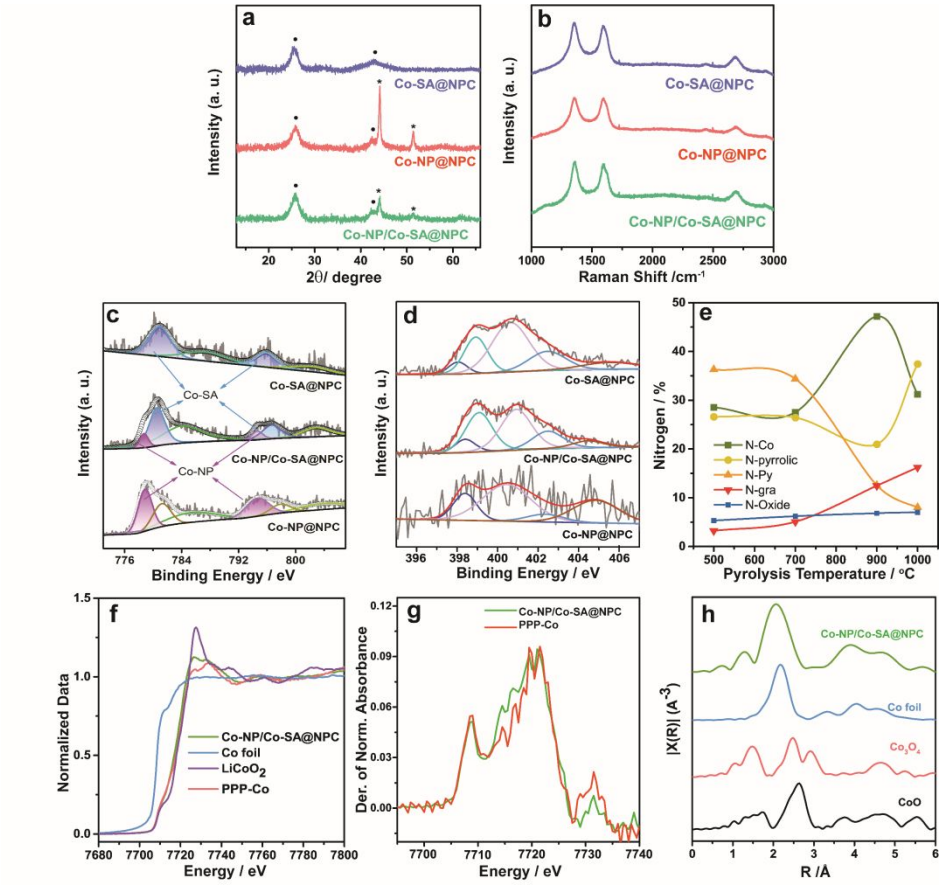

Figure 3. Spectroscopic analyses of different **Co-NP/Co-SA@NPC** materials. (a) Powder X-ray diffraction (pXRD) patterns of **Co-NP/Co-SA@NPC**, **Co-SA@NPC**, **Co–NPC**. (b) Raman spectra of the materials. (c,d) High-resolution X-ray photoelectron spectroscopy (XPS) spectra of **Co-NP/Co-SA@NPC**, **Co-SA@NPC**, **Co–NPC**: (c) Co2p (d) N1s. (e) Temperature dependency of the nitrogen content of thermolyzed samples of **PPP-Co**. (f) Normalized K-edge XANES spectra of **Co-NP/Co-SA@NPC**, Co foil, $LiCoO_2$, and **PPP-Co**. (g) First derivative XANES spectra of **Co-NP/Co-SA@NPC** and **PPP-Co**. (h) FT-EXAFS spectra of **Co-NP/Co-SA@NPC** and standard samples, Co foil, Co_2O_3 and CoO.

Several metal centers within the porphyrin backbone of the metallated porphyrin polymer undergo structural rearrangement during high-temperature pyrolysis, resulting in the formation of cobalt nanoparticles, **Co-NP**, although a proportion of CoNx sites remain due to the inherent stability of the porphyrin macrocycle.[56] The presence of cobalt nanoparticles catalyzes graphitization,[57] leading to the formation of multilayer graphitic shells encapsulating the nanoparticles (Figure 2d). This graphitic coating serves as a protective layer, minimizing electrical contact resistance, facilitating efficient intercomponent electron transfer, and preventing the oxidation of metallic cobalt nanoparticles.[58]

Atom-level structural features of **Co-NP/Co-SA@NPC** were investigated using aberration-corrected high-angle annular dark-field scanning TEM (ac-HAADF-STEM). As shown in Figure 2i, a moderate number of scattered bright dots (indicated by yellow circles; see also Figure S5) are present corresponding to cobalt single atom (**Co-SA**) sites (identified as being CoN_4 species; vide infra) distributed throughout the carbon matrix. HR-TEM (Figure S5a) of **Co-SA@NPC** shows graphitic nanorings about pores formed by acid etching of the cobalt nanoparticles. For comparison, see Figure S5b where Co-NP immobilized between several layers of graphitic carbon can be observed for **Co-NP@NPC**. Lattice fringes consistent with the proposed structures were observed at 0.21 and 0.34 nm, respectively, corresponding to Co(111) and graphitic C(002). **PPP-Co** exhibited no SAED or XRD peaks consistent with its essentially amorphous structure and lack of **Co-NP**.

Other salient analyses of the materials are shown in Figure 3. The pXRD pattern of **Co-NP/Co-SA@NPC** (Figure 3a) contains two broad peaks at 26° and 43° due to the (002) and (101) lattice planes of graphitic carbon.[59] Peaks at 44.1° and 51.4° are respectively associated with the (111) and (200) planes of metallic fcc **Co-NP** (JCPDS No. 15-0806). Peaks due to **Co-NP** are absent in samples pyrolyzed below 1000 °C indicating that nanoparticle formation occurs only at or above this temperature. Graphitic carbon peaks are also absent in samples thermolyzed between 500-700 °C indicating the importance of higher temperatures (900 °C and above) for graphitization (Figure S6a). Additionally, the absence of graphitic structures in **PPP-1000** suggests that cobalt promotes graphitization (Figure S7). The pXRD pattern of **Co-NP@NPC** is similar to that of **Co-NP/Co-SA@NPC** indicating the presence of graphitic carbon and **Co-NP**, and the pXRD pattern of **Co-SA@NPC** contains only broad peaks assignable to graphitic carbon confirming the absence of **Co-NP**. Thus, the form and composition of **Co-**

NP/Co-SA@NPC are strongly affected by the presence of cobalt and the thermolysis temperature, which both promote graphitization.

Raman spectra of the materials (Figure 3b) contain two intense peaks around 1350 and 1580 cm^{-1} assigned as D and G bands, respectively ('D' indicates disordered carbon, 'G' is due to in-plane vibrations of sp^2 graphitic carbon). An additional peak at 2750 cm^{-1} corresponds to the 2D band of multilayered graphitic structures.[60] Materials thermolyzed below 1000 °C or without Co contained very weak or no 2D peak confirming the necessity of the two conditions for the formation of the multilayered graphitic structure. Raman spectra of **Co-SA@NPC** and **Co-NP@NPC** similarly contain D, G, and 2D bands. The relative intensity ratio of D and G (I_d/I_g) indicates the degree of disorder in the carbon structure with values of 1.02, 1.01, and 1.0 calculated for **Co-SA@NPC**, **Co-NP/Co-SA@NPC** and **Co-NP@NPC** respectively. The small increase in I_d/I_g is due to nanoparticle formation.[61,62]

X-ray photoelectron spectroscopy (XPS) measurements were performed to gain insight into the chemical composition and oxidation states of the materials' components. Figure S8a shows the XPS survey spectrum of **PPP-Co** with Co $2p_{1/2}$ and Co $2p_{3/2}$ at 795.7 and 780.3 eV, respectively (Figure S8b). The N1s spectrum (Figure S8c) is dominated by a peak at 399.16 eV peak which corresponds to the nitrogen-cobalt coordinate bond.[59] Figure 3c,d shows the high-resolution Co 2p and N 1s XPS spectra of **Co-NP/Co-SA@NPC** where peaks at 778.7 and 794.6 eV correspond to Co $2p_{3/2}$ and $2p_{1/2}$ of metallic cobalt Co0. Peaks at 780.5 and 796.4 eV correspond to Co^{2+} at cobalt single atom sites (CoN_4) with those at 784.04 and 802.8 eV being shakeup satellite peaks. Samples thermolyzed at lower temperatures and **Co-SA@NPC** contained no XPS peaks due to metallic Co consistent with the absence of nanoparticles found by pXRD. (Figure S7) XPS spectra of **Co-NP@NPC** contain peaks due to metallic cobalt (**Co-NP**) at 778.7 and 794.6eV for Co $2p_{3/2}$ and Co $2p_{1/2}$, respectively. The XPS spectrum of **Co-NP/Co-SA@NPC** was deconvoluted with five peaks (Figure 3d) at 398.4, 399.1, 400.9, 402.5, 404.4 eV corresponding respectively to pyridinic N, N-Co, pyrrolic nitrogen, graphitic nitrogen, and N-oxide, confirming nitrogen coordination of cobalt at single atom sites. (Figure S9) Variation in the nitrogen contents with increasing temperature (Figure 3e) revealed a decrease in N-Co and an increase in pyrrolic nitrogen above 900 °C due to aggregation of cobalt as cobalt nanoparticles and the resulting decline in availability of **Co-SA** single atom sites. An increase in the graphitic nitrogen content is found as the temperature increases from 500 – 900 °C (Figure S10). Interestingly, in the case of **Co-NP@NPC**, nitrogen content was found to be significantly reduced. This is caused by loss of nitrogen during thermolysis due to the absence of single-atom sites where nitrogen might be retained in **NPC**. Furthermore, the absence of an N-Co peak confirms the absence of single-atom catalysts in **Co-NP@NPC**. In contrast, deconvolution of the nitrogen peaks in **Co-SA@NPC** revealed a similar pattern to that of **Co-NP/Co-SA@NPC** due to the retention of nitrogen in the structure and cobalt single atoms after etching of the cobalt nanoparticles.

To investigate the electronic structure and coordination environment of **Co-NP/Co-SA@NPC** at the atomic level, X-ray absorption near-edge structure (XANES) and extended X-ray absorption structure (EXAFS) experiments were conducted at the Co K-edge. Figure 3f shows the XANES spectrum of **Co-NP/Co-SA@NPC**, which has a characteristic Co K-edge absorption located between those of Co foil and $LiCoO_2$ indicating Co oxidation states ranging from Co^0 to Co^{2+}. Furthermore, the first derivative of the XANES pre-edge data (Figure 3g) shows a distinctive peak in the energy range 7710 to 7715 eV, corresponding to the $1s \rightarrow 4p^z$ transition of in-plane Co^{II}-N_4 moieties.[63] The EXAFS spectrum (Figure 3h) contains a characteristic peak due to Co^0-Co^0 bonds configured at 2.1 Å, further confirming the presence of Co metallic nanoparticles. A characteristic Co-N peak was also observed at 1.37 Å. A slight shift in the Co^0-Co^0 peak (relative to Co foil) in EXAFS and a XANES peak 7727 eV for **Co-NP/Co-SA@NPC** is probably due to the strong interaction between **Co-NP** and **Co-SA** sites. Overall, the physical and chemical analyses suggest a close integration of cobalt single-atom species and metallic cobalt nanoparticle in **Co-NP/Co-SA@NPC** which is combined within a graphitic porous structure. These key features of **Co-NP/Co-SA@NPC** promote its catalytic activity for ORR with a strong likelihood of synergetic effects.[64,65]

ORR catalytic activities of the **Co-NP/Co-SA@NPC** catalyst and other materials were evaluated by using electrochemical methods (Figure 4) Cyclic voltammetry (CV) of **Co-NP/Co-SA@NPC** measurements at a scan rate of 25 mV s^{-1} in 0.1 M KOH solution (Figure 4a) in nitrogen or oxygen saturated electrolyte using a three-electrode setup. For N_2 saturated electrolyte, no significant redox peaks were observed. However, for O_2 saturated electrolyte, a strong cathodic response was observed demonstrating the excellent intrinsic catalytic ability of **Co-NP/Co-SA@NPC** as catalyst for electrochemical reduction of oxygen. To further investigate, linear sweep voltammetry (LSV; Figure 4b, Table S1) was conducted in an oxygen-saturated 0.1 M KOH solution using a catalyst-modified rotating disk electrode (RDE) as the working electrode. The optimal thermolysis temperature for the materials was determined by comparing the ORR performance of electrocatalysts prepared at different temperatures. (Figure S11, Table S2) Of the materials prepared, **Co-NP/Co-SA@NPC** prepared at 1000 °C, exhibits superior ORR catalytic performance with an onset potential (E_{onset}) of 0.96 V vs RHE (reversible hydrogen electrode) and a half-wave potential ($E_{1/2}$) of 0.865 V vs RHE, the latter value being similar to Pt/C (20 wt%). However, as observed from the polarization curve, the mixed (kinetic + diffusion) region potential window for **Co-NP/Co-SA@NPC** is narrower than that of Pt/C, inferring better prospects for practical use in methanol-based fuel cell.[66] Of the other materials tested, **PPP-Co** and **PPP-Co/500** exhibit low ORR activity due to ineffective development of the materials' structures especially a lack of graphitization. **PPP-1000** (Figure. S12) shows a 75 mV lower half-wave potential compared to **Co-NP/Co-SA@NPC** reflecting the importance of cobalt for efficient electrocatalysis by boosting ORR activity.

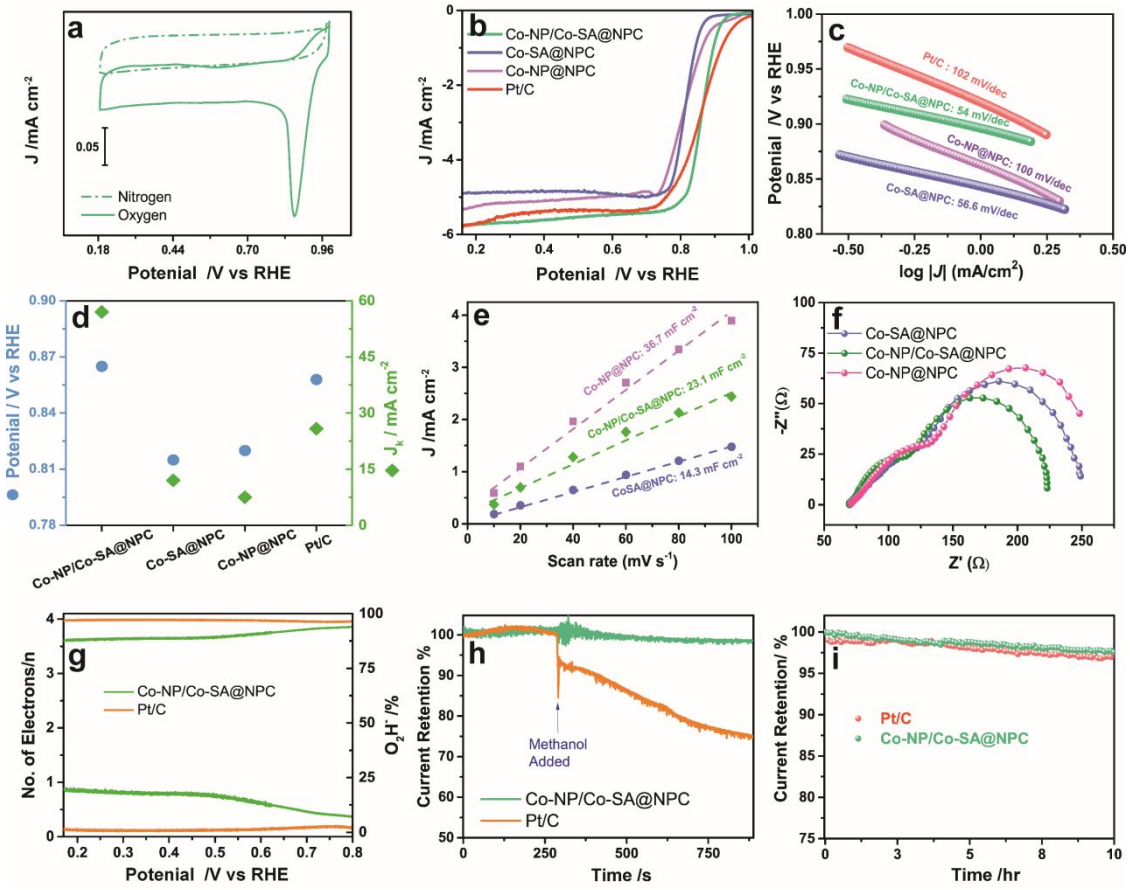

Figure 4. Electrochemical characterization of **Co-NP/Co-SA@NPC**. (a) Cyclic voltammograms under N_2 (dashed line) and O_2 (solid line). (b) Linear sweep voltammetry (LSV) curves and (c) the corresponding Tafel plots. (d) $E_{1/2}$ and J_k values for the electrocatalyst materials and Pt/C. (e) Electrical double layer capacitance, C_{dl} and (f) Nyquist plot of the electrocatalysts measured at 1600 rpm in a 0.1 M KOH electrolyte. (g) $\%HO_2^-$ and electron transfer number determined by RRDE at a scan rate of 10 mV s^{-1}. (h) Methanol crossover and (i) evaluation of durability based on the i–t chronoamperometric responses of **Co-NP/Co-SA@NPC** and Pt/C.

The effects of cobalt single atoms and nanoparticles were studied using the control electrocatalysts, **Co-SA@NPC** and **Co-NP@NPC**. Considering the LSV curves (Figure 4b), it was found that **Co-NP/Co-SA@NPC** exhibits a 50 mV more positive half-wave potential than **Co-SA@NPC** (0.815 V vs RHE) indicating that cobalt nanoparticles enhance significantly the electrocatalytic activity. $E_{1/2}$ of the nanoparticle-only **Co-NP@NPC** is 45 mV lower than **Co-NP/Co-SA@NPC** emphasizing the importance also of the copresence of cobalt single atoms and cobalt nanoparticles including possible synergetic effects. The excellent ORR activity of **Co-NP/Co-SA@NPC** can be further confirmed by Tafel plots (Figure 4c) and considering kinetic current density (J_k). As shown in Figure 4d, **Co-NP/Co-SA@NPC** exhibits an excellent J_k value of 57 mA/cm^2 at 0.8 V, which is more than double that of **Pt/C**. Also, the Tafel slope of **Co-NP/Co-SA@NPC** is 54.5 mV dec^{-1}, suggesting favorable ORR kinetics on **Co-NP/Co-SA@NPC** (Figure 4c) Interestingly, **Co-SA@NPC** has a Tafel slope (56.6 mV dec^{-1}) similar to **Co-NP/Co-SA@NPC**, while that of **Co-NP@NPC** (100 mV dec^{-1}) denotes comparatively slow reaction kinetics and is similar to Pt/C. This suggests that, while both **Co-SA** and **Co-NP** enhance ORR efficiency, the role of **Co-SA** is to improve reaction kinetics.

The intrinsic electrocatalytic activity was investigated using impedance spectroscopy and electrochemical double-layer capacitance (C_{dl}), a quantity directly related to the electrochemical active surface area, based on the cyclic voltammetry (CV) curves at different scan rates (Figure S13). **Co-NP/Co-SA@NPC** exhibits a high C_{dl} value of 23 mF cm^{-2}, indicating a larger electrochemical surface area than for **Co-SA@NPC** (C_{dl} = 14.3 mF cm^{-2}), although it is lower than that of **Co-NP@NPC** (C_{dl} = 36.7 mF cm^{-2}) (Figure 4e). This indicates a larger number of catalytically active sites for **Co-NP/Co-SA@NPC** over **Co-SA@NPC** due to the etching of cobalt nanoparticles. Nyquist plots of the materials (Figure 4f) indicate that **Co-NP/Co-SA@NPC** has the lowest charge transfer resistance (58 Ω), compared to **Co-NP@NPC** (91.4 Ω) and **Co-SA@NPC** (90.18 Ω) suggesting better charge transfer than occurs in the other materials under the same conditions.

Rotating ring disk electrode (RRDE) tests (Figure 4g) show an electron transfer number for ORR by **Co-NP/Co-SA@NPC** at 3.8, indicating a dominant four-electron pathway for ORR. Notably, the peroxide yield calculated for **Co-NP/Co-SA@NPC** is well below 15 % within the potential window 0.2 to 0.8 V. Compared to other cobalt electrocatalysts derived from porphyrins,[56,67,68] **Co-NP/Co-SA@NPC** exhibits a higher electron transfer number and lower peroxide yield, owing to the rational design and synergy of structural components. As expected, **Co-SA@NPC**

also shows a higher peroxide yield compared to **Co-NP/Co-SA@NPC**.

To elucidate the direct involvement of single-atom active sites in promoting the ORR activity, a poisoning test was performed using NaCN which is known to block M–Nx centers.[69,70] As shown in Figure S14, poisoning decreases the half-wave potential and limits current density for **Co-NP/Co-SA@NPC**, **Co-NP@NPC** and **Co-SA@NPC**. **Co-NP/Co-SA@NPC** undergoes an 86 mV drop in its half-wave potential; for **Co-SA@NPC**, 69 mV reduction is observed. Also, it is interesting to note that the reduction in diffusion-limited current is prominent for **Co-SA@NPC** (27 % drop) and **Co-NP@NPC** (13.7 %) compared to **Co-NP/Co-SA@NPC** (7.5 % drop), suggesting excellent poisoning tolerance of the electrocatalyst. Poisoning tolerance might arise from a higher density of active sites, which can compensate for the losses caused by poisoning. Additionally, the graphitic carbon structure provides a physical barrier, preventing direct contact between the poisoning agent and the active sites. These results suggest that the high ORR activity of **Co-NP/Co-SA@NPC** can be attributed to a synergetic effect, due to the copresence of single atom centres and cobalt nanoparticles. Methanol tolerance and durability are also important aspects for the practical implementation of the catalyst. Figure 4h shows that **Co-NP/Co-SA@NPC** maintains a stable current density even after injection of 3M methanol, whereas Pt/C exhibits a sharp decrease in current density due to methanol oxidation. Additionally, as shown in Figure 4i, **Co-NP/Co-SA@NPC** retains a significant percentage of its initial current density after 10 h of continuous operation, indicating the excellent durability of the catalyst. The high durability of the catalyst (is attributed to its resistance to peroxide and effective protection especially of the **Co-NP** sites provided by the multilayered graphitic structure. A comprehensive comparison of activity, selectivity and stability of recent state-of-the-art non-precious metal catalysts is shown inn Table S4 showcasing the excellent performance of **Co-NP/Co-SA@NPC**. The remarkable methanol tolerance and excellent durability (see also Supplementary Information Figures S15–S17) of the **Co-NP/Co-SA@NPC** electrocatalyst along with superior performance compared to other cobalt-based catalysts highlight its strong potential for practical applications.

Although **Co-NP/Co-SA@NPC** is a mixed component material having a broad range of environments for each of its active elements including wide-ranging separating distances of the active sites, we have assessed their relative contributions, especially **Co-NP** and **Co-SA**, using computational methods. In particular, synergies between active sites are not easy to detect even if experimental data indicates that such mechanisms are operating. For computational purposes, an N-doped graphene (**NPC**) structure containing the three most common nitrogen defects observed in graphene (pyrrolic, pyridinic and graphitic) was constructed (see Figure S18a). **Co-SA** sites can be formed by incorporating a Co atom into a void provided by an N4 defect (Figure S18b), which is a remnant of the starting porphyrin material. A thirteen Co atom icosahedral nanoparticle was also constructed using the Atomic Simulation Environment (ASE) toolkit, and was incorporated on **NPC**. The formation energies of **NPC** and **Co-SA** on N-doped graphene (**Co-SA@NPC**) and **Co-NP** on **NPC** (**Co-NP@NPC**) were calculated using the following equations:

$$E_f\,(\mathbf{NPC}) = E_{total}\,(\mathbf{NPC}) - E(\text{graphene}) - 3.5 * E(N_2) \quad [1]$$

$$E_f\,(\mathbf{Co\text{-}SA@NPC}) = E_{total}\,(\mathbf{Co\text{-}SA@NPC}) - E_{total}\,(\mathbf{NPC}) - E(\mathbf{Co}) \quad [2]$$

$$E_f(\mathbf{Co\text{-}NP@NPC}) = E_{total}\,(\mathbf{Co\text{-}NP@NPC}) - E_{total}\,(\text{NPC}) - E_{icosahedron}(\text{Co}) \quad [3]$$

where, E_{total} (**NPC**), E_{total} (**Co-SA@NPC**) and E_f (**Co-NP@NPC**) are the total energies obtained during relaxation of **NPC**, **Co-SA@NPC** and **Co-NP@NPC** structures, respectively. $E(N_2)$, E(Co) and $E_{icosahedron}$(Co) are the energies of nitrogen molecules, Co atom in the nanoparticle structure and one unit of Co_{13} icosahedron, respectively. E_f (**NPC**), E_f (**Co-SA@NPC**) and E_f (**Co-NP@NPC**) are the formation energies of **NPC**, **Co-SA@NPC** and **Co-NP@NPC**, respectively.

To study the oxygen reduction reaction (ORR) activity on the resulting systems, an associative mechanism involving a $4e^-$ transfer process in an alkaline medium[71] was explored:

$$O_2(g) + * \rightarrow O_2* \quad [4]$$

$$O_2* + H_2O\,(l) + e^- \rightarrow HOO* + OH^- \quad [5]$$

$$HOO* + e^- \rightarrow O* + OH^- \quad [6]$$

$$O* + H_2O\,(l) + e^- \rightarrow HO* + OH^- \quad [7]$$

$$HO* + e^- \rightarrow OH^- + * \quad [8]$$

Initially, the key intermediates for ORR reaction O*, OH* and OOH* are adsorbed on **Co-SA@NPC** at five distinct sites, namely C1, C2, C3, C4 and C5 (Figure 18b). The adsorption energies for all five sites were calculated using the following equations:

$$\Delta E_{ads}(HOO*) = E_{total}(HOO*) - [E* + 2E(H_2O) - 1.5E(H_2)] \quad [9]$$

$$\Delta E_{ads}(O*) = E_{total}(O*) - [E* + E(H_2O) - E(H_2)] \quad [10]$$

$$\Delta E_{ads}(HO*) = E_{total}(HO*) - [E* + E(H_2O) - 0.5E(H_2)] \quad [11]$$

where ΔE_{ads}(HO*), ΔE_{ads}(O*) and ΔE_{ads}(HOO*) are the adsorption energies of HO*, O* and HOO* intermediates, respectively. E_{total}(HO*), E_{total}(O*) and E_{total}(HOO*) are the total energies of the system, E* is the energy of the system without intermediate, $E(H_2O)$ and $E(H_2)$ are the energy of the reference molecules.

Figure S19 shows the adsorption energy profile of ORR intermediates adsorbed over five distinct sites. However, the adsorption energy is relatively large for all the cases. This is expected because of the electronegative nature of nitrogen which inhibits adsorption on carbon as well as at Co. In view of these matters, new structures to study reactions on **Co–SA@NPC** and **Co-NP@NPC** were prepared (Figure S20) involving the binding of **Co-SA** at a single pyridinic-N defect site. Intermediates *OH, *O and *OOH species were adsorbed over Co site in reconstructed **Co-SA@NPC** (Figure S20a) and reconstructed **Co-NP@NPC** (Figure S20b). The free energy profile is shown in Figure 5. Free energy of the O* intermediate over Co in **Co-NP@NPC** is lower than that in **Co-SA@NPC** (Figure 5) with Bader charges of –0.79 and –0.58, respectively (Table

S3). The oxygen intermediate is strongly bound at the hollow site formed by three cobalt atoms of **Co-NP** (Figure S21). Hence, it experiences greater charge accumulation than its **Co-SA** counterpart. Similarly, O atoms in HO* and HOO* intermediates are saturated with three Co atoms (Figure S21). This saturation leads to stronger interaction of these intermediates with **Co-NP** making desorption difficult. This is reflected in the free energy plots where the overpotential for **Co-NP@NPC** is greater than for **Co-SA@NPC**. However, both systems show negative free energy at U = 1.23 V. Hence, **NPC** structures with **Co-SA** and **Co-NP** can accelerate the ORR process more effectively than the individual systems.

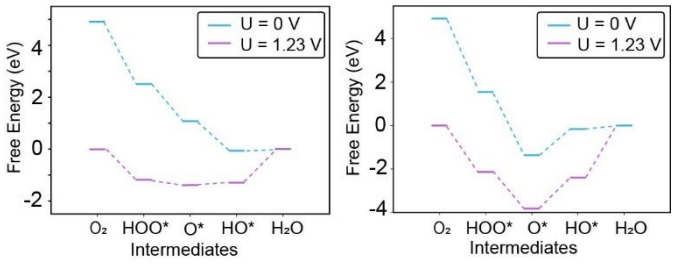

Figure 5. Gibbs free energy plots for oxygen reduction reaction for **Co-SAC@NPC** (left) and **Co-NP@NPC** (right).

Conclusions

In summary, we have developed a facile, low-cost synthesis of ORR-active electrocatalyst, which is highly scalable based on its ease of operation, and produces poisoning-resistant materials with ORR performance ostensibly superior to Pt/C. The synthesis protocol involves Friedel-Crafts polymerization/ metalation/thermolysis and leads to the electrocatalyst **Co-NP/Co-SA@NPC** consisting of N-doped graphene embedded with single cobalt atoms in the copresence of cobalt nanoparticles and with an ultralow loading of Co (0.3 at%). The composition of the material has been investigated in-depth allowing a deeper understanding of its electrochemical properties and usefulness as an electrocatalyst. Remarkably, the **Co-NP/Co-SA@NPC** catalyst exhibits an ORR half-wave potential of 0.865 V vs RHE, surpassing the performance of commercial 20 wt% Pt/C catalyst and competitive with other reported ORR catalysts (see Table S4). Furthermore, the **Co-NP/Co-SA@NPC** electrocatalyst exhibits superior durability and methanol tolerance compared to Pt/C. Computational analysis supports possible synergetic effects in **Co-NP/Co-SA@NPC** where the copresence of **Co-NP/Co-SA** can accelerate ORR processes. Overall, the scalable synthesis method and excellent properties of this catalysts pave the way for the future development of high-performance cobalt-based electrocatalysts for ORR in industrial applications, especially alkaline fuel cell devices.

Author contributions

J.P.H. conceived and managed the experiments. **A.S.** designed and performed the experiments. **A.S**, **A.P.** and **R.N.** carried out electrochemical measurements and analyses. **A.S.**, **A.P.** and **N.V.** undertook preliminary characterization and data interpretation. **J.H.**, **O.C.** and **R.M.** conducted TEM/HR-TEM/HAADF-STEM microcscopy. **J.X.** and **K.K.** performed the synchrotron-based X-ray measurements and the related data analyses. **P.G.**, **A.K.S.** and **R.N.** designed and performed computational analysis. **A.S**, **J.P.H** and **G.J.R** prepared and revised the figures. **A.S.** and **J.P.H.** wrote the manuscript. **L. K. S.**, **K.A.** and **Y.Y.** supported and revised the manuscript. All authors have contributed to writing the manuscript and have given approval to the final version of the manuscript.

Conflicts of interest

There are no conflicts to declare.

Data availability

The data supporting this article have been included as part of the ESI.†

Acknowledgements

The authors are grateful to the JST-ERATO Yamauchi Materials Space-Tectonics Project (JPMJER2003), and the Queensland Node of the Australian National Fabrication Facility (ANFF-Q). R.N. and Y.Y. acknowledge financial support from the Japan Society for the Promotion of Science (JSPS No. P22063). J.X. is grateful to the National Institute for Materials Science, International Center for Young Scientists, Japan (ICYS, NIMS) for an ICYS fellowship and research funds). This research was also partly supported by World Premier International Research Center Initiative (WPI Initiative), MEXT, Japan. N.V. is grateful for financial support from the Japan Society for the Promotion of Science (JSPS) for a JSPS postdoctoral fellowship (JSPS No. P21764) supported by JSPS KAKENHI Grant Number JP22KF0385. This study was also partially supported by the Japan Society for the Promotion of Science KAKENHI Grant Numbers, JP20H00392 and JP23H05459

Notes and references

1 J. Zhang, Z. Xia and L. Dai, *Sci. Adv.* 2023, **1**, e1500564.
2 Z. W. Seh, J. Kibsgaard, C. F. Dickens, I. Chorkendorff, J. K. Nørskov and T. F. Jaramillo, *Science* 2017, **355**, eaad4998.
3 X. Tian, X. Zhao, Y.-Q. Su, L. Wang, H. Wang, D. Dang, B. Chi, H. Liu, E. J. M. Hensen, X. W. Lou and B. Y. Xia, *Science* 2019, **366**, 850–856.
4 R. Zeng, Y. Yang, X. Feng, H. Li, L. M. Gibbs, F. J. DiSalvo and H. D. Abruña, *Sci. Adv.* 2023, **8**, eabj1584.
5 Y. Zhou, G. Chen, Q. Wang, D. Wang, X. Tao, T. Zhang, X. Feng and K. Müllen, *Adv. Funct. Mater.* 2021, **31**, 2102420.
6 E. Jung, H. Shin, B.-H. Lee, V. Efremov, S. Lee, H. S. Lee, J. Kim, W. H. Antink, S. Park, K.-S. Lee, S.-P. Cho, J. S. Yoo, Y.-E. Sung and T. Hyeon, *Nat. Mater.* 2020, **19**, 436–442.
7 J. Li, M. Chen, D. A. Cullen, S. Hwang, M. Wang, B. Li, K. Liu, S. Karakalos, M. Lucero, H. Zhang, C. Lei, H. Xu, G. E. Sterbinsky, Z. Feng, D. Su, K. L. More, G. Wang, Z. Wang and G. Wu, *Nat. Catal.* 2018, **1**, 935–945.

8 Z. Kong, T. Liu, K. Hou and L. Guan, *J. Mater. Chem. A.* 2022, **10**, 2826–2834.
9 J. Li, W. Xia, J. Tang, Y. Gao, C. Jiang, Y. Jia, T. Chen, Z. Hou, R. Qi, D. Jiang, T. Asahi, X. Xu, T. Wang, J. He and Y. Yamauchi, *J. Am. Chem. Soc.* 2022, **144**, 9280–9291.
10 H. Tan, J. Tang, J. Kim, Y. V. Kaneti, Y.-M. Kang, Y. Sugahara, and Y. Yamauchi, *J. Mater. Chem. A* 2019, **7**, 1380–1393.
11 S. Yasuda, A. Furuya, Y. Uchibori, J. Kim and K. Murakoshi, *Adv. Funct. Mater.* 2016, **26**, 738–744.
12 P. M. Usov, B. Huffman, C. C. Epley, M. C. Kessinger, J. Zhu, W. A. Maza and A. J. Morris, *ACS Appl. Mater. Interfaces* 2017, **9**, 33539–33543.
13 R. Jiang, L. Li, T. Sheng, G. Hu, Y. Chen and L. Wang, *J. Am. Chem. Soc.* 2018, **140**, 11594–11598.
14 M. Kim, K. L. Firestein, J. F. S. Fernando, X. Xu, H. Lim, D. V. Golberg, J. Na, J. Kim, H. Nara, J. Tang and Y. Yamauchi, *Chem. Sci.* 2022, **13**, 10836–10845.
15 O. Y. Bisen, R. Nandan, G. Raj, A. K. Yadav and K. K. Nanda, *ACS Appl. Energy Mater.* 2022, **5**, 14019–14034.
16 H. Yabu, K. Nakamura, Y. Matsuo, Y. Umejima, H.Matsuyama, J. Nakamura and K. Ito, *ACS Appl. Energy Mater.* 2021, **4**, 14380–14389.
17 Y. Wu, Z. Jiang, X. Lu, Y. Liang and H. Wang, *Nature* 2019, **575**, 639–642.
18 X. Li, H. Lei, J. Liu, X. Zhao, S. Ding, Z. Zhang, X. Tao, W. Zhang, W. Wang, X. Zheng and R. Cao, *Angew. Chem. Int. Ed.* 2018, **57**, 15070–15075.
19 I. Liberman, R. Shimoni, R. Ifraemov, I. Rozenberg, C. Singh and I. Hod, *J. Am. Chem. Soc.* 2020, **142**, 1933–1940.
20 W. Fan, Z. Duan, W. Liu, R. Mehmood, J. Qu, Y. Cao, X. Guo, J. Zhong and F. Zhang, *Nat. Commun.* 2023, **14**, 1426.
21 H. Lei, C. Liu, Z. Wang, Z. Zhang, M. Zhang, X. Chang, W. Zhang and R. Cao, *ACS Catal.* 2016, **6**, 6429–6437.
22 W. Xia, Z. Hou, J. Tang, J. Li, W. Chaikittisilp, Y. Kim, K. Muraoka, H. Zhang, J. He, B. Han and Y. Yamauchi, *Nano Energy* 2022, **94**, 106868.
23 M. Zhao, Y. Wang, Q. Ma, Y. Huang, X. Zhang, J. Ping, Z. Zhang, Q. Lu, Y. Yu, H. Xu, Y. Zhao and H. Zhang, *Adv. Mater.* 2015, **27**, 7372–7378.
24 D. Feng, Z.-Y. Gu, J.-R. Li, H.-L. Jiang, Z. Wei and H.-C. Zhou, *Angew. Chem. Int. Ed.* 2012, **51**, 10307–10310.
25 R. Wang, X. Wang, W. Weng, Y. Yao, P. Kidkhunthod, C. Wang, Y. Hou and J. Guo, *Angew. Chem. Int. Ed.* 2022, **61**, e202115503.
26 Z. Xiang, Y. Xue, D. Cao, L. Huang, J.-F. Chen and L. Dai, *Angew. Chem. Int. Ed.* 2014, **53**, 2433–2437.
27 J. Chen, D. Wu, Z. Zhou and Y. Huang, *Int. J. Hydrogen Energy* 2021, **46**, 27576–27584.
28 X. Li and Xiang, Z. *Nat. Commun.* 2022, **13**, 57.
29 Z. Liao, Y. Wang, Q. Wang, Y. Cheng and Z. Xiang, *Appl. Catal. B* 2019, **243**, 204–211.
30 J. Yuan, S. Chen, Y. Zhang, R. Li and J. Zhang, *Adv. Mater.* 2022, **34**, 2203139.
31 S. Lin, C. S. Diercks, Y.-B. Zhang, N. Kornienko, E. M. Nichols, Y. Zhao, A. R. Paris, D. Kim, P. Yang, O. M. Yaghi and C. J. Chang, *Science* 2015, **349**, 1208–1213.
32 H. Lei, Q. Zhang, Z. Liang, H. Guo, Y. Wang, H. Lv, X. Li, W. Zhang and U.-P. Apfel, *Angew. Chem. Int. Ed.* 2022, **61**, e202201104.
33 I. Hijazi, T. Bourgeteau, R. Cornut, A. Morozan, A. Filoramo, J. Leroy, V. Derycke, B. Jousselme and S. Campidelli, *J. Am. Chem. Soc.* 2014, **136**, 6348–6354.
34 B.-Q. Li, S.-Y. Zhang, B. Wang, Z.-J. Xia, C. Tang and Q. Zhang, *Energy Environ. Sci.* 2018, **11**, 1723–1729.
35 B.-Q. Li, S.-Y. Zhang, X. Chen, C.-Y. Chen, Z.-J. Xia and Q. Zhang, *Adv. Funct. Mater.* 2019, **29**, 1901301.
36 J. Zhu, H. Zhou, C. Zhang, J. Zhang and S. Mu, *Nanoscale* 2017, *9*, 13257–13263.
37 Y. Jia, L. Zhang, L. Zhuang, H. Liu, X. Yan, X. Wang, J. Liu, J. Wang, Y. Zheng, Z. Xiao, E. Taran, J. Chen, D. Yang, Z. Zhu, S. Wang, L. Dai and X. Yao, *Nat. Catal.* 2019, **2**, 688–695.
38 R. Liu, C. von Malotki, L. Arnold, N. Koshino, H. Higashimura, M. Baumgarten and K. Müllen, *J. Am. Chem. Soc.* 2011, **133**, 10372–10375.
39 C. Han, Q. Li, D. Wang, Q. Lu, Z. Xing and X. Yang, *Small* 2018, **14**, 1703642.
40 Y. Yin, J. Wang, T. Li, J. P. Hill, A. Rowan, Y. Sugahara and Y. Yamauchi, *ACS Nano* 2021, **15**, 13240–13248.
41 Z. Yang, J. Yang, H. Niu, J. Hui, H. Chen and M. Xiang, *Energy Storage* 2022, **4**, e313.
42 L. Peng, Y. Sun, S. Guo and C. Li, *J. Mater. Chem. A* 2022, **10**, 3820–3821.
43 H. Xu, H. Jia, H. Li, J. Liu, X. Gao, J. Zhang, M. Liu, D. Sun, S. Chou, F. Fang and R. Wu, *Appl. Catal. B* 2021, **297**, 120390.
44 Y. Lian, K. Shi, H. Yang, H. Sun, P. Qi, J. Ye, W. Wu, Z. Deng and Y. Peng, *Small* 2020, **16**, 1907368.
45 W. Li, L. Wu, X. Wu, C. Shi, Y. Li, L. Zhang, H. Mi, Q. Zhang, C. He and X. Ren, *Appl. Catal. B* 2022, **303**, 120849.
46 W.-W. Zhao, P. Bothra, Z. Lu, Y. Li, L.-P. Mei, K. Liu, Z. Zhao, G. Chen, S. Back, S. Siahrostami, A. Kulkarni, J. K. Nørskov, M. Bajdich and Y. Cui, *ACS Appl. Energy Mater.* 2019, **2**, 8605–8614.
47 W. Chaikittisilp, N. L. Torad, C. Li, M. Imura, N. Suzuki, S. Ishihara, K. Ariga and Y. Yamauchi, *Chem. Eur. J.* 2014, **20**, 4217–4221.
48 R. Nandan, P. Pandey, A. Gautam, O. Y. Bisen, K. Chattopadhyay, M.-M. Titirici and K. K. Nanda, *ACS Appl. Mater. Interfaces* 2021, **13**, 3771–3781.
49 X. Han, X. Ling, D. Yu, D. Xie, L. Li, S. Peng, C. Zhong, N. Zhao, Y. Deng and W. Hu, *Adv. Mater.* 2019, **31**, 1905622.
50 M. F. Sanad, A. R. P. Santiago, S. A. Tolba, M. A. Ahsan, O. Fernandez-Delgado, M. S. Adly, E. M. Hashem, M. M. Abodouh, M. S. El-Shall, S. T. Sreenivasan, N. K. Allam and L. Echegoyen, *J. Am. Chem. Soc.* 2021, **143**, 4064–4073.
51 L. Bai, C.-S. Hsu, D. T. L. Alexander, H. M. Chen and X. Hu, *J. Am. Chem. Soc.* 2019, **141**, 14190–14199.
52 H. Huang, D. Yu, F. Hu, S.-C. Huang, J. Song, H.-Y. Chen, L. L. Li and S. Peng, *Angew. Chem. Int. Ed.* 2022, **61**, e202116068.
53 D. Yu, Y. Ma, F. Hu, C.-C. Lin, L. Li, H.-Y. Chen, X. Han and S. Peng, *Adv. Energy Mater.* 2021, **11**, 2101242.
54 K. J. Msayib and N. B. McKeown, *J. Mater. Chem. A* 2016, **4**, 10110–10113.
55 Z.-S. Wu, L. Chen, J. Liu, K. Parvez, H. Liang, J. Shu, H. Sachdev, R. Graf, X. Feng and K. Müllen, *Adv. Mater.* 2014, **26**, 1450–1455.
56 W. Orellana, C. Z. Loyola, J. F. Marco and F. Tasca, *Sci. Rep.* 2022, **12**, 8072.
57 M. Zhang, C. Wang, R. Luo, W. Zhang, S. Chen, X. Yan, J. Qi, X. Sun, L. Wang and J. Li, *J. Mater. Chem. A* 2019, **7**, 5173–5178.
58 R. S. Weatherup, L. D'Arsié, A. Cabrero-Vilatela, S. Caneva, R. Blume, J. Robertson, R. Schloegl and S. Hofmann, *J. Am. Chem. Soc.* 2015, **137**, 14358–14366.
59 Z. Xiang, Y. Xue, D. Cao, L. Huang, J.-F. Chen and L. Dai, *Angew. Chem. Int. Ed.* 2014, **53**, 2433–2437.
60 P. Kumar, K. Kannimuthu, A. S. Zeraati, S. Roy, X. Wang, X. Wang, S. Samanta, K. A. Miller, M. Molina, D. Trivedi, J. Abed, M. A. Campos Mata, H. Al-Mahayni, J. Baltrusaitis, G. Shimizu, Y. A. Wu, A. Seifitokaldani, E. H. Sargent, P. M. Ajayan, J. Hu and M. G. Kibria, *J. Am. Chem. Soc.* 2023. **145**, 8052–8063.
61 H. Guo, Q. Feng, J. Zhu, J. Xu, Q. Li, S. Liu, K. Xu, C. Zhang and T. Liu, *J. Mater. Chem. A* 2019, **7**, 3664–3672.
62 F. Kong, X. Cui, Y. Huang, H. Yao, Y. Chen, H. Tian, G. Meng, C. Chen, Z. Chang and J. Shi, *Angew. Chem. Int. Ed.* 2022, **61**, e202116290.

63 Y. He, Q. Shi, W. Shan, X. Li, A. J. Kropf, E. C. Wegener, J. Wright, S. Karakalos, D. Su, D. A. Cullen, G. Wang, D. J. Myers and G. Wu, *Angew. Chem. Int. Ed.* 2021, **60**, 9516–9526.
64 J. Zhang, Y. Xie, Q. Jiang, S. Guo, J. Huang, L. Xu, Y. Wang and G. Li, *J. Mater. Chem. A* 2022, **10**, 16920–16927.
65 M. Zhang, H. Li, J. Chen, F.-X. Ma, L. Zhen, Z. Wen and C.-Y. Xu, *Adv. Funct. Mater.* 2023, **33**, 2209726.
66 R. Nandan, O. Y. Bisen and K. K. Nanda, *J. Phys. Chem. C* 2021, **125**, 10378–10385.
67 Y. Sun, L. Silvioli, N. R. Sahraie, W. Ju, J. Li, A. Zitolo, S. Li, A. Bagger, L. Arnarson, X. Wang, T. Moeller, D. Bernsmeier, J. Rossmeisl, F. Jaouen and P. Strasser, *J. Am. Chem. Soc.* 2019, **141**, 12372–12381.
68 K. Dong, J. Liang, Y. Ren, Y. Wang, Z. Xu, L. Yue, T. Li, Q. Liu, Y. Luo, Y. Liu, S. Gao, M. S. Hamdy, Q. Li, D. Ma and X. Sun, *J. Mater. Chem. A* 2021, **9**, 26019–26027.
69 M. Kim, D.-H. Nam, H.-Y. Park, C. Kwon, K. Eom, S. Yoo, J. Jang, H.-J. Kim, E. Cho and H. Kwon, *J. Mater. Chem. A* 2015, **3**, 14284–14290.
70 O. Y. Bisen, R. Nandan, G. Raj, A. K. Yadav and K. K. Nanda, *ACS Appl. Energy Mater.* 2022, **5**, 14019–14034.
71 R. Ma, G. Lin, Y. Zhou, Q. Liu, T. Zhang, G. Shan, M. Yang and J. Wang, *NPG Comput. Mater.* 2019, **5**, 78.

The data supporting this article have been included as part of the ESI.†